International Journal of
ENGINE RESEARCH

Analysis of the interaction of Spray G and in-cylinder flow in two optical engines for late gasoline direct injection

Christopher Geschwindner[1], Patrick Kranz[2], Cooper Welch[1], Marius Schmidt[1], Benjamin Böhm[1], Sebastian A Kaiser[2] and Joaquin De la Morena[3] (iD)

Abstract

An investigation of the interaction between the in-cylinder flow and the spray topology in two spray-guided direct injection optical engines is reported. The bulk flow field in the combustion chamber is characterized using particle image velocimetry. Geometrical parameters such as the axial penetration and the spray angle of the liquid spray are measured using Mie scatter imaging and/or diffuse back-illumination. The measured parameters are compared with data from a constant volume chamber available in the literature. For a late injection strategy, the so-called ECN Spray G standard condition, the mean values of the spray penetration do not seem to be significantly perturbed by the in-cylinder flow motion until the plumes approach the piston surface. However, spray probability maps reveal that cycle-to-cycle fluctuations of the spatial distribution of the liquid spray are affected by the magnitude of the in-cylinder flow. Particle image velocimetry during injection shows that the flow field in the vicinity of the spray plumes is heavily influenced by air entrainment, and that an upward flow in-between spray plumes develops. Consistent with previous research that demonstrated the importance of the latter flow structure for the prevention of spray collapse, it is found that increased in-cylinder flow magnitudes due to increased intake valve lifts or engine speeds enhance the spray-shape stability. Compared with cases without injection, the influence of the spray on the in-cylinder flow field is still noticeably approximately 2.5 ms after the start of injection.

Introduction

In recent years, engine development for passenger car applications has moved toward spark-ignition direct injection (SIDI). Stratified-charge direct injection offers the potential to improve efficiency in part-load operation by reducing pumping losses due to throttling. In stratified SIDI, engine load can be controlled solely by the amount of fuel injected in the high-pressure fuel injection. However, proper mixture preparation is required to provide reliable ignition and reduce emissions.[1] In the beginning, SIDI engines used a wall-guided combustion system, in which the spray was directed toward a shaped piston providing a flammable mixture around the centrally located spark plug.[2] Recently, spray-guided combustion systems have been developed which have advantages with regard to particle emissions,[3] since one of the most significant causes of such emissions is wall-wetting at the piston surface.[4]

The injectors for spray-guided SIDI engines are custom-designed to provide the desired penetration,

[1]Fachgebiet Reaktive Strömungen und Messtechnik (RSM), Technische Universität Darmstadt, Darmstadt, Germany
[2]Institute for Combustion and Gas Dynamics – Reactive Fluids (IVG-RF), University of Duisburg-Essen, Duisburg, Germany
[3]CMT-Motores Térmicos, Universitat Politècnica de València, Valencia, Spain

Corresponding author:
Joaquin De la Morena, CMT-Motores Térmicos, Universitat Politècnica de València, Camino de Vera, s/n, Edificio 6D, E-46022 Valencia, Spain.
Email: joadela@mot.upv.es

droplet size distribution, and fuel–air mixing while avoiding wall-wetting. However, engine parameters such as the bulk-gas pressure and temperature during injection or the in-cylinder flow have a strong influence on the spray characteristics. The injection timing, for example, is a critical parameter linked to the interplay between injector and engine operation. For a stable engine operation using spray-guided stratified combustion, misfire limits the injection timing window.[5] As Oh and Bae[5] have shown, a trade-off between efficiency and emissions can be observed in which retarded injection timing increases not only the indicated mean effective pressure but also soot emissions.

Even though the spray atomization process is of importance in reducing wall-wetting and hence particulate mass emissions,[6–8] the complex interaction of the fuel injection (injection pressure and injector characteristics) with the in-cylinder flow also needs to be considered, as shown by Stiehl et al.[9] for hollow-cone injectors and by Piock et al.[10] for multi-hole injectors. Fuel injection and mixture preparation have been investigated for stratified engine operation as summarized in a review article by Fansler et al.[11] Optical diagnostics have especially helped understand the in-cylinder processes. Sprays have been visualized using high-speed Mie scatter imaging,[12] spark emission spectroscopy can measure fuel concentrations near the spark plug,[13] and laser-induced fluorescence (LIF) of a tracer can image fuel distributions.[14] Tracer-LIF, in combination with simultaneous particle image velocimetry (PIV) and flame imaging, has helped to understand misfires linked with strong local variations of the equivalence ratio at the spark plug.[14,15] Even though the average flow features were dominated by the effect of the spray momentum,[14] using simultaneous spray visualizations and high-speed PIV, Stiehl et al.[9] showed that the in-cylinder tumble flow has a direct impact on the formation of the spray. Sementa et al.[16] showed differences in the mixture formation for early and late injection strategies, but without decoupling the effects of in-cylinder flow and thermodynamic conditions during the injection. Song and Park[17] linked the effect of strong air motion during the intake with spray atomization.

The interaction between spray plumes of multi-hole injectors is of great interest. For the same injector as used in this work (ECN Spray G), Gutierrez et al.[18] showed that the interaction is stronger when the injection is initiated during the intake stroke than it is in the nearly quiescent environment of a constant volume chamber (CVC). The spray may collapse not only at low in-cylinder pressures, due to flash boiling, but also at increased ambient pressures,[19,20] conditions which occur during the late injection. Mie scattering and Schlieren imaging have been used to quantify the decrease of the angle between the plumes during the injection event indicating spray collapse. A detailed investigation of mixing based on LIF and Rayleigh scattering has shown that the plumes start to merge sooner after the start of injection (aSOI) for increased ambient densities.[21] This transient behavior of the individual plumes during spray collapse was confirmed by Sphicas et al.[22] They performed time-resolved measurements of the spray-surrounding flow field using PIV and showed that ambient gas is entrained axially from the downstream regions of the spray as well as radially through the gap in-between the plumes. Once the neighboring plumes start to interact, this gap closes and the angle between the plumes quickly decreases until full spray collapse.

In order to gain comprehensive knowledge on gasoline direct injection, the engine combustion network (ECN) uses a standardized multi-hole injector geometry—Spray G—accompanied by well-defined ambient conditions.[23] In terms of experimental studies, this injector has already been investigated at various research institutions which have mainly used CVCs. Light scattering techniques have been used to study the topology of the liquid and vapor phases of the spray. Mie scatter imaging[22,24–29] and light extinction measurements, namely diffuse back-illumination (DBI),[22,24,27,30,31] are the most common methods used for imaging the liquid spray, whereas Schlieren imaging is used for the visualization of the vapor phase.[22,24–27,29,31] For example, Hamzah et al.[24] compared the liquid-spray penetrations with the Spray G injector determined by DBI and Mie scatter imaging. In operating points with severe flash boiling, they found that the spray penetration extracted from DBI was greater than from Mie scatter imaging due to beam-steering effects.

In this work, an investigation of the interactions of in-cylinder flow and spray structure is conducted. For this purpose, the Spray G injector is installed in two different optical engines with different in-cylinder flow characteristics. The Spray G standard condition is evaluated, which constitutes a late injection during the compression stroke of engines operated in stratified charge mode. The spray shape, axial penetration, and spray angle are characterized by DBI and right-angle Mie scatter imaging. The spray imaging results are combined with PIV data, providing a better understanding of the spray–flow interactions. In addition, the results obtained with DBI are analyzed and compared with data from the CVC experiments of Payri et al.[31] The experiments in both engine facilities were planned and conducted separately from each other using the boundary conditions of the ECN as a guideline. Differences between the engines were then evaluated afterward. Nevertheless, comparing the spray–flow interaction using the same injector in engines with different but comparable boundary conditions is a meaningful task as the influence of parameters altering the flow and the thermodynamic state of the bulk gas can be investigated. Since a similar experimental approach is used, two linked data sets are compared providing a better understanding of the spray development in engines as a whole.

This article is organized as follows: section "Optical engines and boundary conditions" summarizes the

Table 1. Engine and injector properties.

Parameter	UDE	TUD
Cylinder head configuration	4V pent roof with VVA	4V pent roof
Combustion chamber layout	Centrally mounted injector and spark	Centrally mounted injector and spark
Injector number	AV67-014	AV67-027
Injector angle (°)	0	8
Optical access	73 mm piston window + top 28 mm of stroke + pent roof	75 mm piston window + top 55 mm of stroke + 8 mm in pent roof
Bore × stroke (mm)	84 × 92	86 × 86
Geom. comp. ratio (–)	9:1	8.7:1

UDE: University of Duisburg-Essen; TUD: Technische Universität Darmstadt; VVA: variable valve actuation.
The UDE engine has VVA to change the maximum intake valve lift.

Table 2. Engine operating parameters at each engine facility.

Parameter	Spray G standard		
Facility	UDE	TUD	ECN, CVC[23]
Fuel	Iso-octane	Iso-octane	Iso-octane
Bulk gas	100% N_2 (non-reacting)	Air (RH 1.8%) (non-reacting)	0% O_2 (non-reacting)
Engine speed (rpm)	1200	800/1500	–
Intake valve lift (mm)	4/9	9.5	–
Intake valve opening duration (°CA)	162/226	160	–
Electronic SOI (°CA)	–50	–40/–43	–
Hydraulic SOI (°CA)	–47.75	–38.58/–40.34	–
Electronic pulse duration (ms)	0.681	0.680	0.680
Intake temperature (°C)	80	37	–
Coolant temperature (°C)	80	60	–
Temperature at hyd. SOI (°C)	276/270	257/245	300
Intake pressure (bar)	1.1	0.95	–
Pressure at hyd. SOI (bar)	5.7/5.5	5.6/5.7	6
Gas density at hyd. SOI (kg/m^3)	3.5/3.4	3.7/3.8	3.5
Fuel pressure (bar)	200	200	200
Fuel temperature (°C)	80	60	90
Fuel mass (mg/cycle)	10	10	10

UDE: University of Duisburg-Essen; TUD: Technische Universität Darmstadt; ECN: engine combustion network; CVC: constant volume chamber; RH: relative humidity; CA: crank angle; SOI: start of injection.

main characteristics of the optical engines used in this study and the operating conditions investigated in the experiments. The optical diagnostics and image processing methodologies of PIV, DBI, and Mie scatter imaging are provided in section "Optical diagnostics and image processing." In section "Results and discussion," the results of the experimental study are presented and discussed with regard to the combined approach of in-cylinder flow imaging and visualization of the liquid spray. Finally, section "Conclusion' summarizes the overall outcome of this study.

Optical engines and boundary conditions

Engine experiments with centrally mounted Spray G injectors are performed at two different facilities, University of Duisburg-Essen (UDE) and Technische Universität Darmstadt (TUD). The single-cylinder SIDI engines have different cylinder heads and optical access to the combustion chamber. Table 1 summarizes the main differences between the experimental facilities.

Both engines are four-stroke engines with similar, but slightly different geometries and compression ratios, as shown in Table 1. The injector in the TUD experiment is mounted at an angle of 8° to the cylinder's central axis while the injector in the UDE engine is mounted vertically. In both engines, the plumes were oriented in the "primary orientation" as specified by the ECN.[23] Optical access is given through the flat piston window and a fused-silica cylinder liner of each engine. The field of view (FOV) is limited by this optical access.

This work assigns 0 °CA (crank angle) as compression top-dead center (TDC), that is, CAs during intake and compression are negative. If not explicitly stated, start of injection (SOI) is always the hydraulic start, when fuel first visibly exits the nozzle outlet.

The operating conditions are summarized in Table 2. The UDE experiments are carried out with variations in intake valve lift (IVL), while in the TUD experiments the engine speed is varied to introduce variations in the in-cylinder flow. The Spray G standard condition (Spray G1) of the ECN, as shown in Table 2, consisting
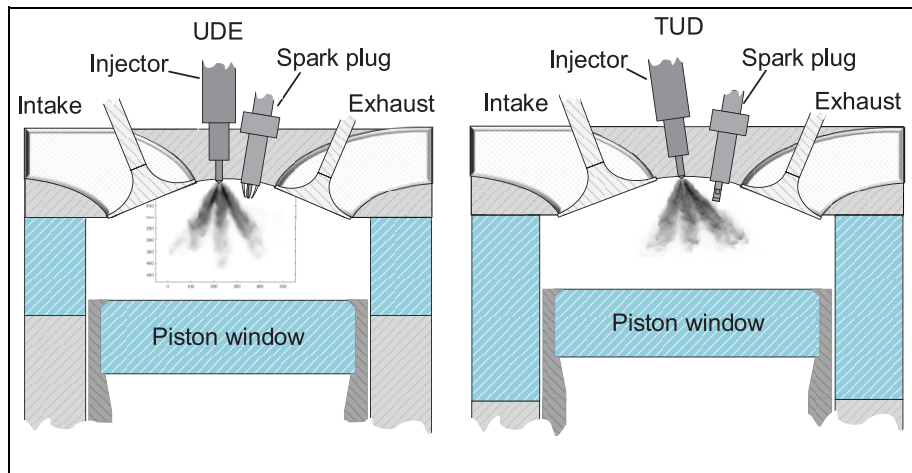
Figure 1. Sketch of the combustion chambers of the optical SIDI engines at UDE and TUD. A grayscale snapshot from Mie scatter imaging is shown in each sketch.

of a late injection during the compression stroke, is targeted. In an engine, the bulk-gas density and temperature can only be pre-estimated before and then be calculated after the experiment with improved accuracy based on the measured pressure trace. In addition, differences in experimental facilities induce further variations in parameters such as the fuel temperature.

However, the main differences in the injection parameters are the hydraulic SOI timing of the engines and the in-cylinder pressure and temperature at hydraulic SOI. The pressure in the intake, exhaust, and cylinder is measured with sub-CA resolution, whereas the intake and exhaust temperatures are measured with lower temporal resolution. To estimate the bulk-gas densities during injection, adiabatic compression with a variable isentropic coefficient is applied to the pressure traces, with the initial temperature estimated as the arithmetic mean of the intake and coolant temperature.

Figure 1 shows a sketch of the combustion chambers of the engines. Both engines' pent-roof cylinder heads have two intake and two exhaust valves. In all images in this work, the intake valves are located on the left, and the exhaust valves on the right of the injector nozzle as shown in the schematics in Figure 1.

The UDE engine, shown in the left panel of Figure 1, has optical access to the top 28 mm of the stroke plus the pent-roof combustion chamber. The flat-topped piston is in the FOV after −60 °CA. It provides optical access to the combustion chamber through a quartz window of 73 mm in diameter. A mass flow controller supplies the engine with gaseous N_2 at a constant intake pressure of 1.1 bar. The temperatures of the coolant, fuel, and intake flow are all set to 80 °C to improve the accuracy of estimating the starting temperature of the adiabatic compression calculation through which the conditions at SOI are determined. Also, 80 °C was chosen for consistency with previous measurements. The combination of intake pressures and temperatures lead to Spray G standard

conditions in the combustion chamber when electronic SOI is at –50 °CA, corresponding to hydraulic SOI at −47.75 °CA. In this work, IVLs of 4 and 9 mm at an engine speed of 1200 rpm are investigated as shown in Table 2. Further details on the engine facility can be found in previous publications.[32–35]

The right panel of Figure 1 illustrates the TUD engine configuration. In contrast to UDE, the TUD engine has optical access to the top 55 mm of the stroke plus 8 mm in the pent-roof combustion chamber. The flat-topped piston with a window of 75 mm diameter is in the FOV after −95 °CA. In the current study, the engine is operated with air at an intake pressure of 0.95 bar. The coolant temperature is kept at 60 °C to be consistent with previous studies. The TUD engine has a fixed IVL of 9.5 mm and is operated at both 800 and 1500 rpm in this study. The electronic SOIs are set to –40 °CA for 800 rpm and –43 °CA for 1500 rpm resulting in hydraulic SOIs of –38.58 °CA for 800 rpm and –40.34 °CA for 1500 rpm. A detailed description of the engine facility can be found in Baum et al.[36]

Optical diagnostics and image processing

Gas velocity

Optical arrangement. PIV is a well-known technique to measure instantaneous velocity fields in engines. Figure 2 shows a schematic of the PIV arrangements used in this study. The equipment is summarized in Table 3.

In both experimental facilities, the beam of a double-pulsed neodymium-doped yttrium aluminum garnet (Nd:YAG) laser, frequency doubled to 532 nm, is guided through a combination of a telescope and a negative cylindrical lens to form a light sheet. The inter-pulse delay Δt is adjusted for each CA to achieve optimal particle shifts and to minimize out-of-plane losses. Δt increases from 2 μs during intake to 20 μs toward

Table 3. Equipment and processing parameters for PIV in the TUD and UDE engines.

	UDE	TUD
Camera	PCO Edge 5.5 sCMOS	(a) Photron Fastcam SA-X2
		(b) Phantom v711
Lens	Nikon f = 50 mm f/5.6 + 52 mm close-up lens	Sigma f = 105 mm f/11 + 20 mm extension
Filter	Polarizing filter + BP532/10 nm	–
Max. FOV (width $\times$ height)	63 $\times$ 38 mm^2	58 $\times$ 63 mm^2
Light source	Nd:YAG (Litron) at 532 nm	Nd:YAG (Edgewave) at 532 nm
Optics	Telescope + −20 mm cyl. lens	−50 mm cyl. + −200 mm cyl. + 1000 mm cyl.
Sheet thickness	1.5 mm	1.3 mm
Rep. rate of camera and light source (Hz)	10	(a) 960 at 800 rpm
		(a) 1800 at 1500 rpm
		(b) 4800 at 800 rpm
		(b) 4500 at 1500 rpm
Processing	*DaVis 8.4*	*DaVis 8.4*
Background correction	(a) Sliding high pass (Butterworth) of nine images	Spatial sliding background of four pixels
	(b) Sliding minimum of nine images	
Vector calculation	(a) Passes 1 and 2:	Passes 1 and 2:
	64 $\times$ 64 pixels with 50% overlap	64 $\times$ 64 pixels with 50% overlap
	Passes 3 and 4:	Passes 3 and 4:
	32 $\times$ 32 pixels with 50% overlap	32 $\times$ 32 pixels with 75% overlap
	(b) Passes 1 and 2:	
	64 $\times$ 64 pixels with 50% overlap	
	Passes 3 and 4:	
	32 $\times$ 32 pixels with 75% overlap	
Spatial resolution of vector field	(a) 1.1 mm window size	(a) 2.02 mm window size
	550 μm vector spacing	504 μm vector spacing
	(b) 1.1 mm window size	(b) 2.54 mm window size
	275 μm vector spacing	635 μm vector spacing

PIV: particle image velocimetry; UDE: University of Duisburg-Essen; TUD: Technische Universität Darmstadt; FOV: field of view; Nd:YAG: neodymium-doped yttrium aluminum garnet.
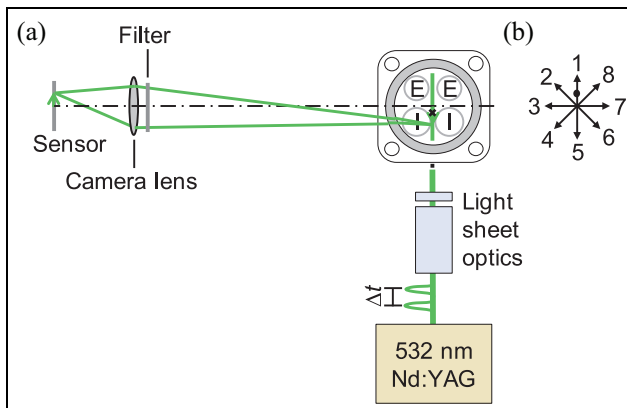For TUD, the equipment used in experiments (a) and (b) is labeled.

Figure 2. (a) Top view of the optical arrangement for flow-field measurements via PIV. (b) Injector plume orientation with respect to the direction of observation. The black dot in (b) represents the orientation of the injector dimple, which points toward the spark plug.

compression TDC. The light sheet is reflected by the 90° mirror vertically through the Bowditch piston assembly and the fused-silica piston window onto the cylinder center axis, as shown in Figure 2. The area near the cylinder liner cannot be illuminated due to clipping by the metal mounting of the quartz piston window.

Dow Corning silicone oil droplets of $\sim$0.5 μm diameter are introduced upstream of the intake pipe of the engines which scatter the light through the fused-silica cylinder liner. In the UDE PIV experiments, a polarizing filter is mounted on the lens to suppress some of the light scattered from the in-cylinder surfaces. An additional 532 nm bandpass filter suppresses the room light.

PIV is performed in both engines in two different experiments (a) and (b). In experiment (a), the flow velocity in motored operation without injection is measured. The imaging repetition rates at TUD and UDE are different as shown in Table 3. In the UDE experiment, CA synchronized measurements of 75 cycles at 10 Hz are performed. Vector fields from the intake valves opening at −360 °CA through −70 °CA in steps of 10 °CA are acquired. Between −65 °CA and TDC, the time steps are refined to 5 °CA. At TUD, data are taken in 148 cycles from −360 °CA to TDC with a spacing of 5 °CA both at 800 and 1500 rpm. Experiment (b) is performed with injection. At UDE, 100 CA synchronized double-frame images at −40 °CA, −35 °CA, and −30 °CA are acquired with 4 mm IVL at 1200 rpm. At TUD, data are taken in 84 cycles from −90 °CA to 0 °CA in steps of 1 °CA for 800 rpm and 2 °CA for 1500 rpm.
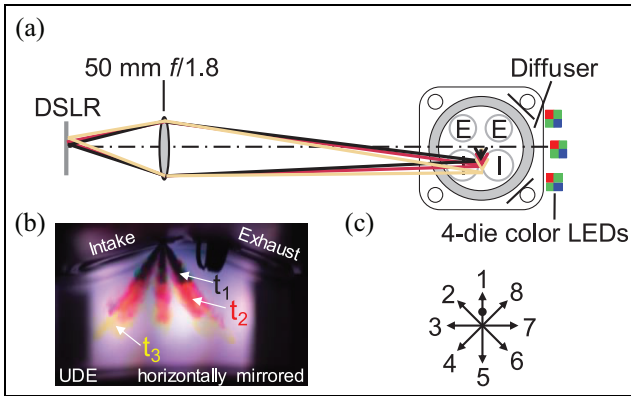
Figure 3. (a) Optical arrangement for diffuse back-illumination applied at UDE. (b) Horizontally mirrored raw color image. Red illumination is at time t_1, green at $t_2 = t_1 + 138.9\,\mu s$, and blue at $t_3 = t_2 + 138.9\,\mu s$. (c) Injector orientation with respect to the camera. The black dot represents the orientation of the injector dimple, which points toward the spark plug.

PIV data post-processing. The software *DaVis 8.4* is used to compute the vector fields with a PIV algorithm. First, a background correction is executed according to the methods summarized in Table 3. Afterward, a geometric mask is applied to each image. The mask removes the combustion chamber contours, piston, and strong reflections in the FOV. Then, algorithmic masking routines (based on calculating the local standard deviation over nine pixels and subsequent thresholding) are used to mask regions full of fuel droplets. The scattering of the fuel droplets cannot be used to compute vectors, since the time delay Δt between laser pulses is not adjusted for the high velocities in the spray and the fuel-droplet density is too high. Therefore, only the gas velocity is represented by the PIV data in this study.

The vector calculations are performed using a multi-pass cross-correlation with decreasing window size (Table 3). The computed vectors are processed further without smoothing. Vectors with a correlation ratio of the first and second peak in each interrogation area below 1.3 are deleted and a universal outlier detection based on a normalized median test in a moving window of 7×7 vectors is applied. The ensemble average at each CA is calculated, rejecting positions with less than 25 valid vectors. In doing so, the average is not biased by a low number of vectors in some regions, especially in the spray region.

Liquid-spray visualization

DBI

Optical arrangement. DBI imaging is one of the standard diagnostics recommended by the ECN for liquid-spray visualization and has been applied to engine sprays several times.[30,31,37] In the current work, DBI is only applied to the spray at UDE.

A schematic of the DBI arrangement is shown in Figure 3(a). It follows the approach of Menser et al.[38]

Three 4-die color light-emitting diodes (LEDs), each with broadband emission at around 600 nm (red, R), 530 nm for two dies (green, G), and 460 nm (blue, B), are used for back-illumination of the liquid spray. Electronic drivers provide power to each die, which are individually gated and delayed. The duration of each gate is adjusted to achieve approximately the same optical pulse intensities. A delay of $\Delta t = 138.9\,\mu s \mathrel{\hat=} 1\,°CA$ between red and green, and of $2 \times \Delta t = 277.8\,\mu s \mathrel{\hat=} 2\,°CA$ between red and blue emission at an engine speed of 1200 rpm is used. This results in a three-image sequence of 7200 frames per second in each observed cycle. The start of illumination is scanned from SOI until 833 μs aSOI.

A quarter section of a sand-blasted Plexiglas cylinder, placed between the LEDs and the fused-silica engine cylinder, diffuses the light to achieve a more homogeneous illumination. The light is then scattered and absorbed by the liquid spray. The remaining signal is detected by a commercial color DSLR camera (Nikon D5300) with a lens of $f = 50$ mm and $f/1.8$. Since the camera has large jitter in the delay between the start of the trigger and the actual exposure, the image acquisition is always initiated at –360 °CA with an exposure time of 100 ms (equal to one whole cycle). The camera is operated at 2 Hz, that is, every fifth engine cycle. Between 11 and 46 color images I and images without injection I_0 are taken phase-locked to a particular CA. Each color image includes information from a burst of three corresponding LED die pulses. An example color image I is shown in Figure 3(b).

DBI data post-processing. As shown in Figure 3(b), the raw images are horizontally mirrored to be consistent with other experiments in this work. Plume 1 is pointing to the exhaust side and plumes 3 and 7 are in the center. The overlapping transmittances between channels of the color filter array on the Bayer sensor are de-mixed[38] and three instantaneous images I_r, I_g, and I_b corresponding to time steps t_1 to t_3 are extracted from the three-channel color image. Afterward, the images are binned in a 4×4 window, that is, the values of 16 pixels are averaged to form one superpixel, reducing the projected pixel size to 57.5 μm. From here on, images with injection are denoted as I, and images without injection (background images) are denoted as I_0.

Analogous to Manin et al.,[27] Beer–Lambert's law for light extinction

$$\frac{I}{I_0} = e^{-\tau} \tag{1}$$

is applied to each image. The pixel-wise division of the measurement I by the background I_0 corrects for inhomogeneities in the illumination and detection path. Then the optical thickness τ is related to the integrated liquid volume fraction $\int_{-y_\infty}^{y_\infty} LVF\,dy$ as

Table 4. Equipment and properties used for the Mie scatter imaging at TUD and UDE engine facilities.

	UDE	TUD
Camera	Nikon D5300	Phantom v711
Lens	Nikon f = 50 mm, f/1.8	Nikon f = 50 mm, f/5.6
Filter	RGGB Bayer color filter array	–
Light source	4-die Color LED (460 nm, 2 × 530 nm, 600 nm)	LED (525 nm)
Optics	Aspherical condenser lenses 25 mm + 100 mm	Aspherical condenser lens 40 mm
Rep. rate (Hz)	2 (three-image sequence per cycle, 7200 Hz)	16,000

TUD: Technische Universität Darmstadt; UDE: University of Duisburg-Essen; LED: light-emitting diode.
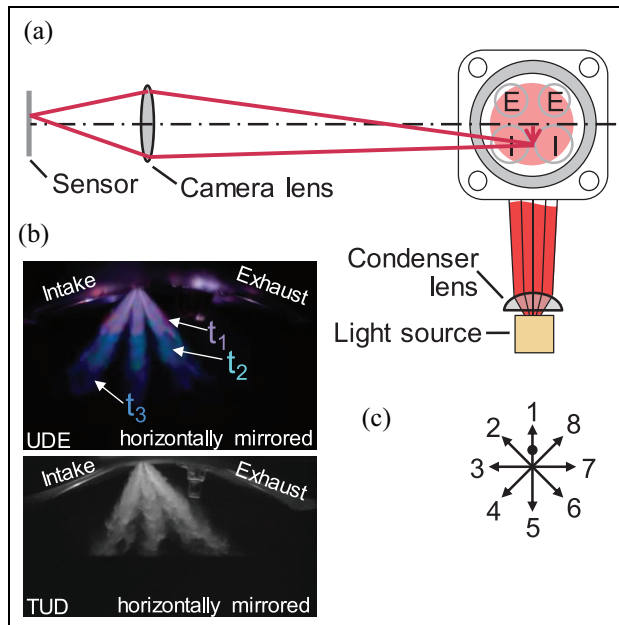
Figure 4. (a) Top view of the optical arrangement for spray visualization via Mie scatter imaging. (b) Horizontally mirrored raw color image (UDE) and gray scale image (TUD). Red illumination is at time t_1, green at $t_2 = t_1 + 138.9\,\mu s$, and blue at $t_3 = t_2 + 138.9\,\mu s$ in the UDE case. (c) Injector plume orientation with respect to the direction of observation. The black dot in (c) represents the orientation of the injector dimple, which points toward the spark plug.

$$\tau = \int_{-y_\infty}^{y_\infty} C^*_{\text{ext, i}} \frac{LVF}{\pi d^3/6}\, dy \Leftrightarrow \int_{-y_\infty}^{y_\infty} LVF\, dy = \tau \frac{\pi d^3/6}{C^*_{\text{ext, i}}}$$

(2)

A droplet diameter d of size 7 μm is used for the calculations, which is based on measurements of the Sauter mean diameter by Parrish et al. for the same injection parameters.[23] The effective extinction cross-section $C^*_{\text{ext, i}}$ is calculated for the three center wavelengths of the color LEDs based on Mie theory as implemented in *MiePlot*[39] for an iso-octane droplet of size d. Here, * denotes a finite collection angle of 350 mrad determined from the optical arrangement. Extinction cross-sections are estimated to be $C^*_{\text{ext, 460 nm}} = 41.7 \times 10^{-6}$ mm, $C^*_{\text{ext, 530 nm}} = 43.2 \times$
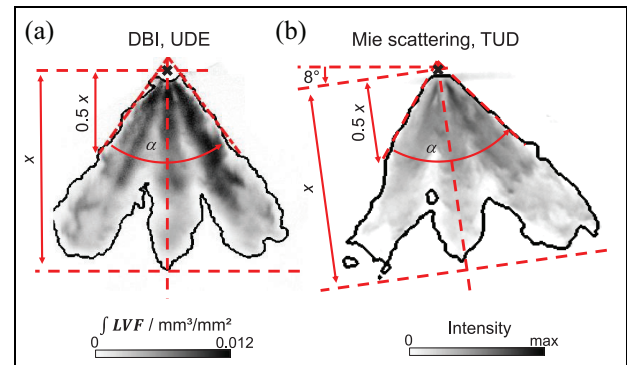

Figure 5. Example single shots from (a) DBI (back-illumination, UDE) and (b) Mie scattering (bottom illumination, TUD) including the detected spray contour shown as a black outline. The spray angle α and the axial penetration x are shown.

10^{-6} mm, and $C^*_{\text{ext, 600 nm}} = 44.4 \times 10^{-6}$ mm for each central emission wavelength. Spray contours are determined by segmenting the images according to Payri et al.[31] with a threshold of 0.2×10^{-3} mm³/mm². An example of the spray contour is shown in Figure 5(a).

Mie scatter imaging

Optical arrangement. In both engines, the spray is also imaged by acquiring Mie scattering of light from a pulsed LED in volume illumination from the bottom through the piston window. Figure 4 shows a schematic of the optical arrangement and example images, while details on the equipment are summarized in Table 4.

At UDE, a four-die color LED (the same as for DBI) is used for this bottom illumination. The operation of LED and camera as well as the FOV and the other imaging parameters are also the same as for DBI. At TUD, a green-light LED system (ILA 5150 GmbH) provides illumination. Here, the LED and camera run at an acquisition rate of 16 kHz, recording 30 images per injection with an inter-frame time of 62.5 μs. The FOV is 80.4 × 60.3 mm² and the projected pixel size is 0.13 mm/pixel. Both camera systems are positioned such that plume 3 points toward the camera as shown in Figure 4(c). Since the Mie scattering illumination is volumetric, the resulting spray images are line-of-sight measurements.

At TUD, an iterative process is used to select the optimal camera lens f-number and LED pulse width by monitoring the changes in the depth of field, exposure intensity, and motion blur. For the present work, the selected LED pulse width is $5\,\mu$s and a lens aperture of $f/5.6$ is used. The camera is focused on a target image plate with a pattern of evenly spaced dots of known dimensions. In addition, a Siemens star is used to verify the focus quality and measure the spatial resolution of the images.

Mie scattering data post-processing. First, the images are dewarped and translated into laboratory coordinates using a calibration target. The RGB Mie scatter images from the UDE experiment are de-mixed as in the DBI processing. The images are then processed using a custom MATLAB code that has three main steps:

1. Masking
All reflective engine features including the cylinder head, intake valves, and the piston are masked out such that the remaining foreground corresponds to Mie scattering of the injected spray.
2. Background subtraction and noise reduction
At TUD, for each injection event, a mean background image generated from three frames before SOI is subtracted. Subsequently, a 3×3 median filter is applied for noise reduction and local homogenization of the spray intensity. At UDE, 4×4 binning is applied, and the images are corrected by a mean background which is obtained without injection.
3. Threshold definition and binarization
For the TUD data, every cycle is assigned an individual threshold s as

$$s = \max\left(I_{\mathrm{bg,\,mean}}\right) + r \cdot \sigma\left(I_{\mathrm{bg,\,mean}}\right) \qquad (3)$$

The first term in this equation is the maximum intensity value of the mean background of three frames before SOI, $I_{\mathrm{bg,\,mean}}$, which remains after the background subtraction. In the second term, in order to have sufficient separation between the remaining background and foreground signal, a separation factor r is multiplied by the two-dimensional (2D) spatial standard deviation σ across $I_{\mathrm{bg,\,mean}}$. Here, r is chosen as 250, which spatially places the segmentation edge in the region of the steep intensity gradient at the spray's boundary. Similarly to the method of Siebers,[40] in which a fixed threshold of 3% of the maximum intensity is applied, strong changes in the separation factor cause only marginal deviations in the measured geometrical parameters of the spray. The values for s vary between 4.9% and 5.6% of the maximum spray intensity in one cycle. As reflections of the scattered spray from the curved fused-silica liner have 3%–4% of the maximum spray intensity, the separation factor ensures that reflections are not taken into account when determining the extent of the liquid spray.

For the UDE data, following the general idea of Siebers,[40] the segmentation threshold is taken as the intensity at the position of the steepest negative gradient in the vertical direction of each frame. To this end, a line plot of 1 mm width (17 pixels) through the injector tip in the axial direction is extracted in each frame. Noise is estimated as three standard deviations calculated in a region of $5 \times 5\,\mathrm{mm}^2$ of a background-corrected image without injection. Pixels with intensities below 3σ are rejected in the line plot. The data are averaged in the y-direction and the derivative is taken in the x-dimension. Then, the intensity at the position of the steepest gradient in the axial direction is extracted for each frame. The threshold intensities (between 2.5% and 10% of the maximum spray intensity) are used to binarize the spray in each image. Finally, 6-pixel erosion followed by 6-pixel dilation is applied to each binarization, and spurious areas of foreground smaller than $17\,\mathrm{mm}^2$ are deleted.

Extraction of geometrical parameters. Geometric parameters of the spray are extracted from the binary images generated by the processing methods for DBI and Mie scatter imaging. Figure 5 illustrates the definitions of the investigated spray features for both experimental approaches. The axial penetration x is defined as the maximum distance of the liquid-spray boundary to the injector tip along the central geometric spray axis. The spray angle α is extracted by a method similar to the one described by Payri et al.[31] The spray contour between 1% and 50% of the axial penetration is extracted and a linear least-squares fit is found. Subsequently, α is the angle between the two fitted lines.

Results and discussion

In-cylinder flow and thermodynamic state in the motored engines

In the first section of the results, the in-cylinder flow in both engines is observed in motored operation without spray injection. The bulk flow structure is evaluated in combination with the thermodynamic state during motored operation to provide a basis for their effects on the spray topology.

Figure 6 shows average velocity fields in motored operation without injection for experiments during the middle of compression (–90 °CA), right before, and after the hypothetical SOI. The figure is organized in terms of increasing velocity magnitudes from left to right. The first and third columns in Figure 6 show results from UDE while the other two are from TUD. The blue–yellow colormap represents the velocity magnitude and the flow directions are displayed by vectors with fixed length. Regions with strong reflections in the background within the FOV are geometrically masked and displayed in white. Thick black lines depict the position of the piston as well as the silhouette of the
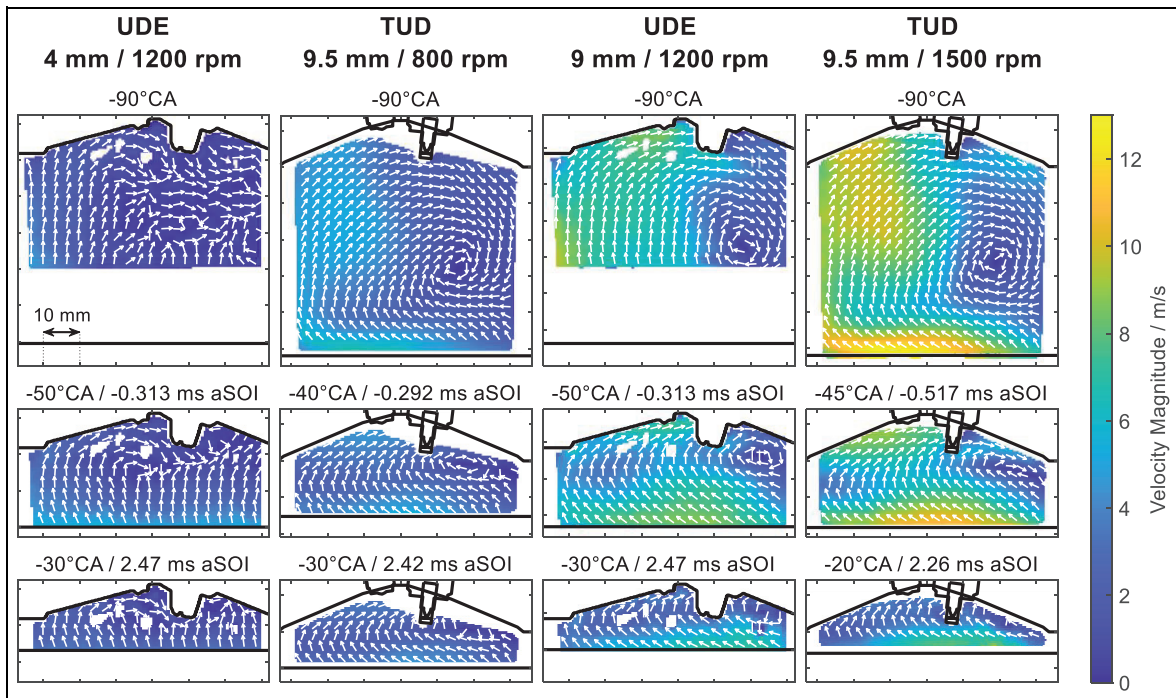
Figure 6. Average vector fields from motored engine experiments without injection. Vector fields from UDE at 1200 rpm with 4 and 9 mm IVL (first and third columns) and from TUD at 800 and 1500 rpm and 9.5 mm IVL (second and fourth columns) are shown for the middle of compression, around SOI, and late during the compression stroke. Every sixth vector is displayed with fixed length.

cylinder head including both the injector and the spark plug. All vector fields are vertically aligned with regard to the position of the injector tip. At –90 °CA, the optical access of the UDE engine limits the FOV as the piston is about 22 mm below the edge of the quartz section of the liner (see Table 1). For the TUD data, the FOV is solely limited by the piston.

At –90 °CA, the 4 mm IVL/1200 rpm case shows low velocity magnitudes and the absence of an apparent tumble vortex. All other cases at –90 °CA display clockwise tumble flow with higher velocity magnitudes on the intake side of the combustion chambers compared with the exhaust side. The magnitude of the tumble flow increases with increasing engine speed and IVL. The highest velocity magnitudes just before SOI, shown in the second row of Figure 6, are located near the piston surface. At 4 mm IVL/1200 rpm, the velocity decreases from the piston to the cylinder head surface, while the remaining results show that the velocity magnitudes first decrease and then increase toward the cylinder head. Finally, late in the compression stroke (the last row in Figure 6), the velocity magnitudes are low, but the tumble can still be seen.

For 4 mm IVL/1200 rpm, the spatially averaged velocity magnitude at –50 °CA is 2.2 m/s. The near-wall velocity, determined as the mean value of the first four rows of velocity data above the piston, is 5.0 m/s, which coincides with the calculated piston velocity of 5.1 m/s. This shows that the tumble-flow energy, initially induced by incoming flow through the intake valve gap, has almost entirely dissipated late in the compression stroke. Therefore, the flow at 4 mm IVL is mainly

induced by the piston movement. Relative to the other velocity data in Figure 6, the 4 mm IVL/1200 rpm case is the most similar to experiments in a CVC. In the same engine at 9 mm IVL, the velocity near the piston surface increases to 7.4 m/s, 48% more than in the 4 mm case. In this engine, increased IVL causes stronger tumble flow preserving the rotational momentum of the intake flow as gas volume is compressed by the piston. Therefore, the in-cylinder velocities for 4 and 9 mm IVL are both affected by the piston but for 9 mm IVL, the tumble is a significant part of the bulk flow.

The variation of the engine speed in the TUD engine from 800 to 1500 rpm increases the mean velocity magnitude above the piston surface from 4.1 to 9.5 m/s, while the instantaneous piston velocity increases from 2.8 to 5.8 m/s for vector fields at –40 °CA and −45 °CA, respectively. At a fixed IVL of 9.5 mm, the intake flow velocity introduced into the combustion chamber at 800 rpm is initially lower and has more time to decelerate during the compression stroke compared with 1500 rpm. At the increased engine speed, higher velocity magnitudes can be observed throughout the entire flow and the overall topology of the velocity field, including the tumble flow, is preserved.

Figure 7 shows the in-cylinder pressure p_{cyl} and bulk-gas density ρ_b during the injection event. ρ_b was calculated via adiabatic compression and the ideal-gas law. The main source of uncertainty here is the start temperature T_0 for adiabatic compression. If $T_0 = 65\,°C$ instead of $T_0 = 80\,°C$ is used, then at –47.75 °CA in the UDE experiment, ρ_b changes from $3.42\,kg/m^3$ (80 °C) to $3.57\,kg/m^3$ (65 °C), a deviation of
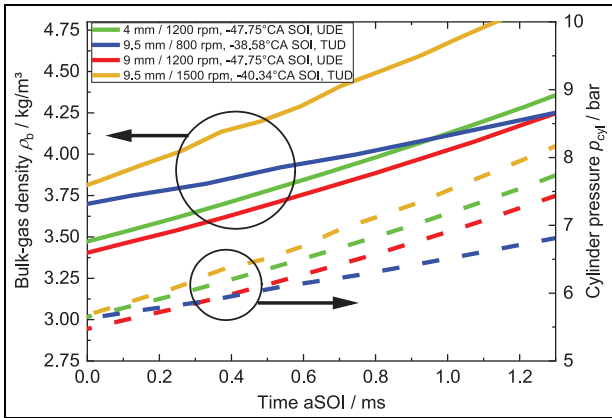
Figure 7. Cylinder pressures p_{cyl} (dashed lines) and bulk-gas densities ρ_b (solid line) calculated via adiabatic compression for all engine operating conditions. The pressure trace is measured with injection. Target values are shown as black arrows for $\rho_{b,target}$ and $p_{cyl,target}$.

4%. Figure 7 also shows that the pressures p_{cyl} at SOI for all experiments are similar but slightly below the ECN target of $p_{cyl,target} = 6$ bar. p_{cyl} develops differently during the injection event due to the differences in IVL, engine speed, adiabatic core temperature T_{ad} (Table 2), and engine designs. The bulk-gas densities ρ_b

at SOI vary in each experiment, since T_{ad} is different in each operating point. ρ_b in the TUD experiment is greater than the target of $\rho_{b,target} = 3.5$ kg/m³ for both engine speeds, while ρ_b in the UDE engine is slightly below the target density at SOI. The case with 9.5 mm IVL/1500 rpm has the strongest change in ρ_b over the course of the injection.

Spray–flow interaction

In the following section, the interaction of the in-cylinder flow and the spray injection is discussed. First, spray imaging data are presented and compared with the bulk flow velocity fields to gain knowledge of the interdependency of the engine speed or IVL and the spray topology. Afterward, PIV data obtained during injection are examined to investigate the spray–flow interaction.

The spatial probability distributions of the liquid-spray area for both the UDE and TUD engines are illustrated in Figure 8. The distributions are generated by adding up the binary images for multiple cycles at the same time aSOI and dividing by the number of cycles. The 2D-probability map displays the likeliness of the liquid spray occurring at a certain pixel visualizing the outlines of the liquid spray as well as cycle-to-cycle variations (CCVs). While distributions from UDE are
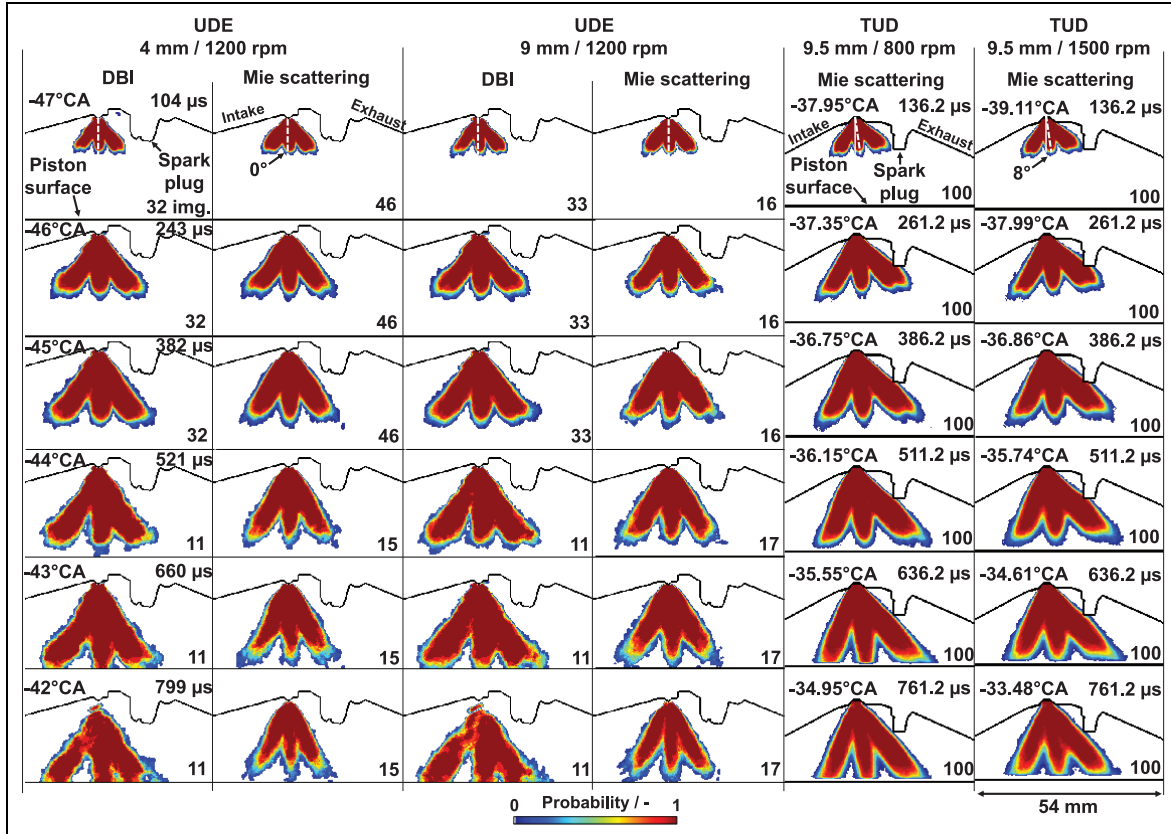

Figure 8. Liquid-spray probability maps as an evolution of the time aSOI from DBI and Mie scatter imaging. The bottom right of each image shows the number of single shots which are used. The first four columns are results from UDE and the remaining two are from TUD.

generated from 11 to 46 non-consecutive injections depending on the observed CA, the probability maps from TUD take 100 consecutive cycles into account.

Comparing the spray outlines from UDE and TUD in Figure 8, the spray inclination of 8° in the TUD experiment can be observed at 136.2 μs aSOI, but the spray outlines are still similar in shape to the ones from the UDE experiments. However, while the central spray axis in the UDE engine points downward vertically without any plumes interacting with the spark plug, the tilted spray in the TUD engine slightly brushes the spark plug whose interference is stronger at 1500 rpm than at 800 rpm. The sprays injected with a vertically mounted injector at 4 mm IVL/1200 rpm as well as at 9 mm IVL/1200 rpm keep their symmetrical shape throughout the observed timespan with minor CCVs. In contrast, the plumes located closer to the exhaust of the TUD engine show a slight deformation over time compared to the plumes closer to the intake.

Due to the late injection strategy, wall impingement can be observed in both engines as the spray expansion is interrupted by the piston top. For the UDE data, contact between the spray and the piston surface occurs between 521 μs aSOI and 660 μs aSOI, while wall impingement in the TUD engine can be observed between 511.2 μs aSOI and 636.2 μs aSOI. Since the ambient gas temperatures in the UDE experiments are above those in the TUD engine (see Table 2), evaporation of the spray takes place faster. This can be noticed in the fading of the liquid spray at 799 μs aSOI in the UDE data compared to the spray outlines of the TUD data that are still maintained at 761.2 μs aSOI.

A comparison of the probability maps of DBI and Mie scattering data in Figure 8 shows that the angle between the two outer plumes obtained from DBI is broader than in the Mie scattering images. In addition, DBI reveals deeper spray penetration than Mie scattering. These differences may be due to several reasons. First, DBI images are corrected for local non-uniformities in illumination and detection, which affects subsequent image segmentation (for detection of the spray outlines) with a global threshold. However, such a correction is not possible for Mie scattering data. Second, the method for determining the thresholds is necessarily different for both diagnostics. Third, it appears that DBI can detect smaller droplets than bottom-illumination Mie scattering. Beam steering is likely negligible in the UDE DBI experiments as determined by the geometrical relations given by Westlye et al.[30] since the emission angle of the light source is greater than the collection angle of the system.

For greater in-cylinder velocity magnitudes (9 mm IVL/1200 rpm and 9.5 mm IVL/1500 rpm), it can be observed that the spray is pushed toward the spark plug. LIF measurements conducted in the UDE engine showed a similar influence of the tumble motion on the

movement of the fully evaporated fuel toward the exhaust of the combustion chamber.[34]

An observation of the CCV of the spray injection by analyzing the probability map at the spray outlines in Figure 8 shows two noticeable effects. First, looking at the temporal evolution of the probability distribution for each engine speed and IVL setting, CCV increases over the course of the spray injection. Early in the injection process, the spray outlines only vary slightly, while with ongoing evaporation at the edge of the liquid spray the probability distribution broadens, indicating increasing CCV. Second, the decrease of the probability at the edges of the spray broadens spatially with increasing flow velocity magnitude, indicating higher CCV in the outlines of the liquid spray with increasing engine speed and IVL. Overall, increasing in-cylinder flow velocities lead to higher fluctuations in the Spray G injection in both engines.

The axial penetration x and penetration velocity $\Delta x/\Delta t$ extracted from DBI and Mie scatter imaging are displayed in Figure 9. In the left column, DBI data from the UDE engine are compared with DBI data from CVC experiments obtained by Payri et al.[31] In the early stages of injection, both axial penetrations in the UDE engine at different IVLs coincide with the penetration measured in the CVC. In the vicinity of the piston surface, the upward flow driven by the piston movement shown in Figure 6 as well as the temporally increasing bulk-gas density decelerates the spray expansion in the axial direction stronger than in the CVC. Still, the deviations between both penetrations measured in the UDE engine at different IVLs are marginal even in the late stages of the injection.

A comparison of the spray penetrations generated from Mie scatter imaging at UDE and TUD is shown in the right column of Figure 9. At the beginning of injection, the axial penetrations in the UDE engine are greater due to the reduced bulk-gas density ρ_b, as shown in Figure 7, which results in higher axial spray velocities compared to the TUD engine. In this early injection phase, the spray's penetration and velocity are mainly determined by the influence of ρ_b on the aerodynamic drag of the spray. Afterward, at 0.28 ms aSOI, the penetration curves of the TUD and UDE data intersect and the spray penetrations at TUD subsequently remain greater. Although the bulk-gas densities for both UDE operating conditions are lower than in the TUD engine for most of the duration of the injection, the penetrations show a different trend to what was found in CVC experiments,[31] where an increase of the bulk-gas density for the Spray G standard condition generally translates into a decrease of the spray penetration. For example, the spray penetration of the operating condition 9.5 mm IVL/800 rpm, although having a higher bulk-gas density, subsequently remains larger than at 9 mm IVL/1200 rpm. As the latter shows a larger upward velocity magnitude, the authors
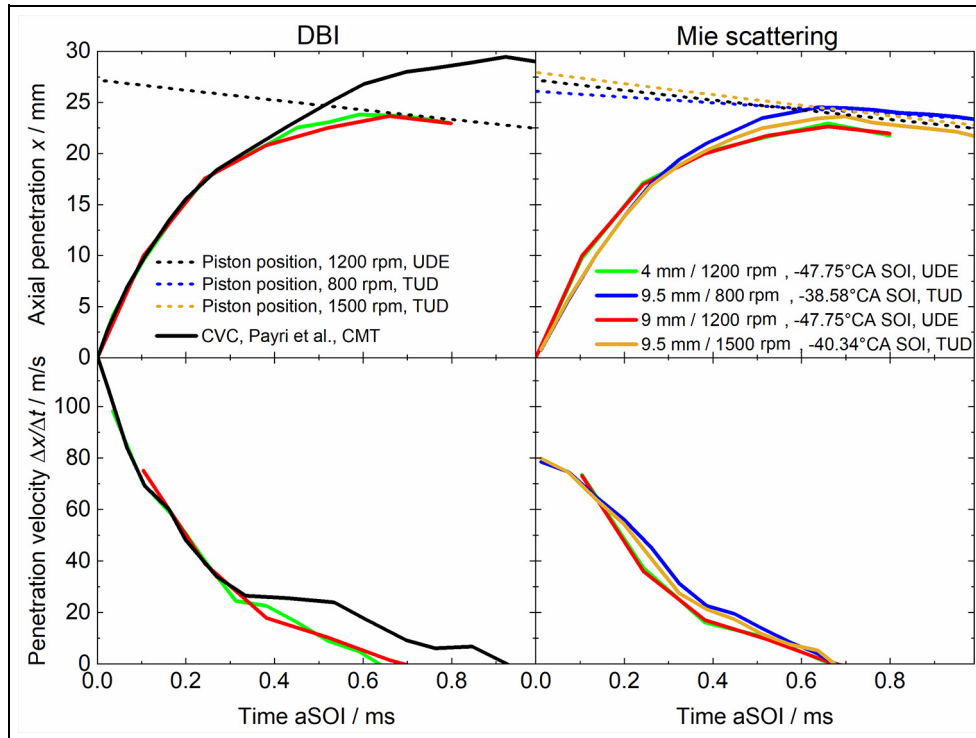
Figure 9. Axial penetration and penetration velocity from DBI and Mie scatter imaging for the Spray G standard condition. DBI results are compared with spray penetration data from the CVC of Payri et al.[31]

conclude that the counter flow decelerates the spray expansion and therefore decreases penetration.

While both axial penetrations of the UDE Mie scattering data show only marginal deviations throughout the entire injection, the two axial penetration curves from the TUD engine separate in the later stages of the injection after 0.28 ms aSOI. For the TUD experiments, this can be explained with the increasing difference between the bulk-gas densities in the late part of the injection and the increased influence of the upward in-cylinder flow above the piston surface at higher engine speeds causing a more pronounced deceleration of the spray penetration.

After discussing the spray imaging data in combination with in-cylinder flow velocity fields in motored operation, the flow structure in the vicinity of the spray is investigated. This allows a more detailed analysis of the spray–flow interaction.

Figure 10 displays the mean velocity fields of the bulk flow after fuel injection. For the UDE engine, data for 4 mm IVL/1200 rpm in the left column are compared to both operating conditions of the TUD engine. Vector fields from both engines are aligned such that the vertical position of the injector tip in each row is equal. Masking is applied to regions with strong reflections within the FOV as well as the spray itself since the scattering by the spray droplets vastly exceeds that by the seeding droplets. The spray appears brighter in the

TUD engine which results in a larger mask for the spray than in the UDE data. Apart from different optical arrangements, this may be due to faster spray evaporation in the UDE engine resulting in less Mie scattering. Masked out areas from fuel droplets are still visible in the TUD engine after 2.416 ms aSOI while the vast majority of fuel in the UDE engine has already evaporated at 1.770 ms aSOI.

The flow fields in the first row of Figure 10 show that a distinctive flow structure is developed which is caused by the injection of the fuel spray. In all cases, air entrainment is visible on the outside of the spray plumes, generating large clockwise vortical structures on the left and counterclockwise on the right side of the spray. At 4 mm IVL/1200 rpm, the velocity of the air entrainment is highest close to the spray plumes, while the results from the TUD engine show slightly lower velocities in the same area. The mask of the spray in the TUD data is larger, hiding velocities as close to the spray plumes as in the UDE data. Furthermore, the spray is inclined in the TUD engine, and therefore, interactions with the in-cylinder flow will be different from those in the UDE engine.

In-between spray plumes, an upward flow is visible in the first row of Figure 10. As the velocity of the in-cylinder flow is increased by altering the IVL and engine speed, the velocity in-between plumes are enhanced similarly. Sphicas et al.[22] have investigated
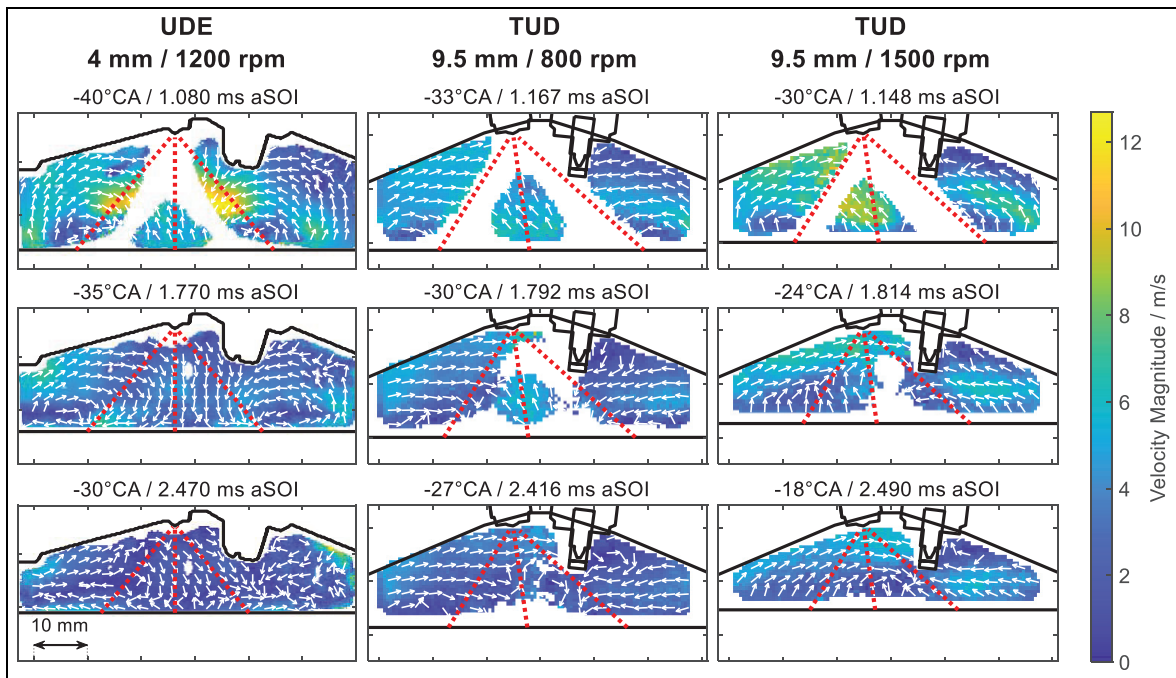
Figure 10. Mean vector fields with injection from three different engine experiments. The scattering of the fuel droplets is masked out in each single shot and a minimum of 25 vectors is required in each position to calculate the mean. The first column is from UDE (mean of 100 fields showing every eighth vector) and the remaining two are from TUD (mean of 84 fields showing every fourth vector). The central injector axis as well as the boundaries of the outer plumes are shown as dashed red lines, the latter representing the full outer spray angle of 40°.[23] Due to problems with the engine hardware, the case 9 mm IVL/1200 rpm from UDE is missing.
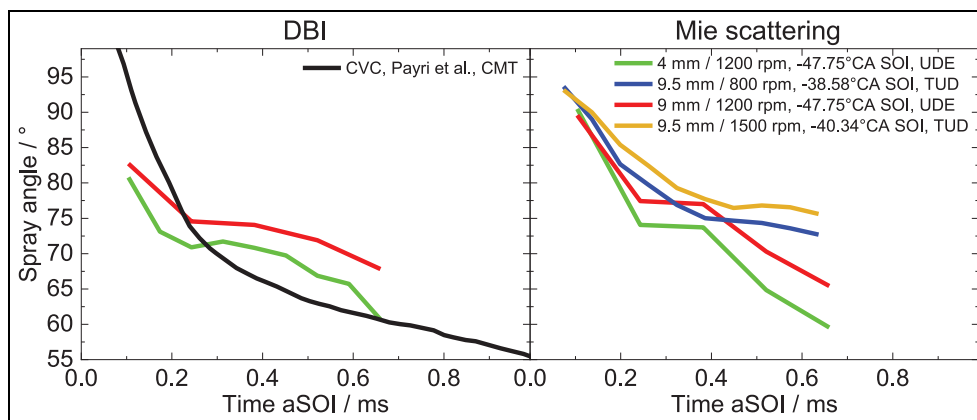

Figure 11. Spray angle from DBI and Mie scatter imaging for the Spray G standard condition. DBI results are compared with data from the CVC.[31]

the flow field between plumes of Spray G in a high-pressure vessel and found that the existence of an upward recirculation between spray plumes is vital in preventing spray collapse. To analyze this behavior in greater depth, the temporal evolution of the spray angle α is depicted in Figure 11. In the left column, DBI data from UDE are compared with CVC data from Payri et al.[31] As the fast decrease of α shows, the spray in the CVC undergoes strong collapse. Initially, the spray angle is greater than measured in both UDE configurations, but by 0.52 ms aSOI it has decreased by 37%. Meanwhile, the spray angles in the UDE engine both begin at lower initial values but only decrease by

13% for 9 mm IVL and 17% for 4 mm IVL in the same timespan, indicating reduced spray collapse at higher in-cylinder flow velocities. Comparing the evolution of the spray angles from the Mie scattering data shown in the right column of Figure 11, the same trend can be observed. The combined analysis of the temporal evolution of the spray angle and the inter-plume flow for engine operation shows that the upward flow during the compression stroke of an engine supports entrainment from areas away from the spray, thereby preventing spray collapse.

After the injection is finished, a strong influence of the spray-induced flow field is still visible in the PIV

data. This is apparent when comparing velocity fields without injection (last row of Figure 6) with velocity fields after injection has taken place (last row of Figure 10) at approximately 2.5 ms aSOI. At 4 mm IVL/1200 rpm, the flow field without injection shows a uniformly upward flow with slight deviations close to the cylinder head. After injection, most of the velocity vectors have reversed their orientation, following the injection direction of the spray to a stagnation point a few millimeters above the piston surface, where the piston-induced velocity direction clashes with the spray-induced air entrainment even after the spray has already evaporated. Also, at 9.5 mm IVL/1500 rpm, the flow structure is disturbed heavily by the spray, but the initial momentum of the tumble is still visible at 2.49 ms aSOI. While for the case of 4 mm IVL/1200 rpm, both spray-induced vortices appear equally strong, the tumble flow at 9.5 mm IVL/1500 rpm causes a more pronounced clockwise rotation in the center of the combustion chamber. This shows that at higher flow velocity magnitudes, the disturbance of the flow field by the injected spray is less severe than at low IVLs and engine speeds.

Conclusion

In this study, the late injection of Spray G in two different optical engines is investigated experimentally. Engine operating parameters and SOI are chosen to fulfill the ambient conditions of the Spray G standard operating condition. The combination of spray imaging using DBI and Mie scattering and flow-field measurements by PIV allows for an analysis of the interaction between the injection and the in-cylinder flow. With increasing IVL and engine speed, in-cylinder flow velocity magnitudes increase. Here, several insights into late injection with the Spray G injector in an engine are gathered:

1. Spatial spray probability distributions revealed that CCVs increase both over the course of the injection and with an increased in-cylinder bulk flow magnitude. Both of these observations are explained by increased turbulent mixing of the spray with the surrounding flow structures.
2. The temporal evolution of axial spray penetrations is only marginally influenced by a variation of bulk flow velocity magnitudes pointing toward a slight decrease of the spray expansion with increased flow-field velocity. A comparison with CVC experiments only shows deviations as the piston approaches the spray, causing wall impingement. Nevertheless, in addition to the increase in bulk gas density, the influence of the in-cylinder flow on the spray development has to be considered in engines operating with late fuel injection.
3. The upward recirculation flow in-between spray plumes is enhanced by the in-cylinder flow with increasing engine speeds and IVLs. This stabilizes the spray shape, preventing unwanted spray collapse induced by plume-to-plume interaction as reported by Sphicas et al.[22]
4. With the SOIs in this study, the in-cylinder flow is heavily disturbed by the spray. If the tumble is weak, it can hardly preserve its initial momentum, yielding to a flow structure that is characterized by two counter-rotating vortices caused by air entrainment during injection. For stronger tumble, more of the initial flow structure survives the injection.

In order to obtain more knowledge on the interactions between in-cylinder flow and spray injection, further investigations have to be conducted, both at the current operating conditions and at other ambient conditions that are defined for Spray G by the ECN.

ORCID iD

Joaquin De la Morena (iD) https://orcid.org/0000-0003-0208-508X

References

1. Alkidas AC. Combustion advancements in gasoline engines. *Energy Convers Manag* 2007; 48: 2751–2761.
2. Costa M, Marchitto L, Merola SS and Sorge U. Study of mixture formation and early flame development in a research GDI (gasoline direct injection) engine through numerical simulation and UV-digital imaging. *Energy* 2014; 77: 88–96.
3. Zhao F, Lai MC and Harrington DL. Automotive spark-ignited direct-injection gasoline engines. *Prog Energy Combust Sci* 1999; 25: 437–562.
4. Moreira ALN, Moita AS and Panão MRO. Advances and challenges in explaining fuel spray impingement:

how much of single droplet impact research is useful? *Prog Energy Combust Sci* 2010; 36: 554–580.

5. Oh H and Bae C. Effects of the injection timing on spray and combustion characteristics in a spray-guided DISI engine under lean-stratified operation. *Fuel* 2013; 107: 225–235.

6. Park C, Kim S, Kim H and Moriyoshi Y. Stratified lean combustion characteristics of a spray-guided combustion system in a gasoline direct injection engine. *Energy* 2012; 41: 401–407.

7. Grover RO, Fansler TD, Lippert A, Drake MC and Assanis DN. A numerical–experimental assessment of wall impingement models for spark-ignition direct-injection engines. *Int J Engine Res.* Epub ahead of print 23 July 2019. DOI: 10.1177/1468087419863966.

8. Ding C-P, Vuilleumier D, Kim N, Reuss DL, Sjöberg M and Böhm B. Effect of engine conditions and injection timing on piston-top fuel films for stratified DISI operation using E30. *Int J Engine Res.* Epub ahead of print 5 September 2019. DOI: 10.1177/1468087419869785.

9. Stiehl R, Schorr J, Krüger C, Dreizler A and Böhm B. In-cylinder flow and fuel spray interactions in a stratified spray-guided gasoline engine investigated by high-speed laser imaging techniques. *Flow, Turbul Combust* 2013; 91: 431–450.

10. Piock WF, Befrui B, Berndorfer A and Hoffmann G. Fuel pressure and charge motion effects on GDi engine particulate emissions. *SAE Int J Engines* 2015; 8(2): 464–473.

11. Fansler TD, Reuss DL, Sick V and Dahms RN. Invited review: combustion instability in spray-guided stratified-charge engines: a review. *Int J Engine Res* 2015; 16: 260–305.

12. Drake MC and Haworth DC. Advanced gasoline engine development using optical diagnostics and numerical modeling. *Proc Combust Inst* 2007; 31: 99–124.

13. Fansler TD, Stojkovic B, Drake MC and Rosalik ME. Local fuel concentration measurements in internal combustion engines using spark-emission spectroscopy. *Appl Phys B* 2002; 75: 577–590.

14. Peterson B, Reuss DL and Sick V. On the ignition and flame development in a spray-guided direct-injection spark-ignition engine. *Combust Flame* 2014; 161: 240–255.

15. Schiffmann P, Reuss DL and Sick V. Empirical investigation of spark-ignited flame-initiation cycle-to-cycle variability in a homogeneous charge reciprocating engine. *Int J Engine Res* 2018; 19: 491–508.

16. Sementa P, Vaglieco BM and Catapano F. Thermodynamic and optical characterizations of a high performance GDI engine operating in homogeneous and stratified charge mixture conditions fueled with gasoline and bio-ethanol. *Fuel* 2012; 96: 204–219.

17. Song J and Park S. Effect of injection strategy on the spray development process in a single-cylinder optical GDi engine. *At Sprays* 2015; 25: 819–836.

18. Gutierrez L, Mansfield AB, Fatouraie M, Assanis D, Singh R, Lacey J, et al. Effects of engine speed on spray behaviors of the engine combustion network "Spray G" gasoline injector. SAE technical paper 2018-01-0305, 2018.

19. Parrish SE, Zhang G and Zink RJ. Liquid and vapor envelopes of sprays from a multi-hole fuel injector operating under closely-spaced double-injection conditions. *SAE Int J Engines* 2012; 5: 400–414.

20. Rachakonda SK, Paydarfar A and Schmidt DP. Prediction of spray collapse in multi-hole gasoline direct-injection fuel injectors. *Int J Engine Res* 2019; 20: 18–33.

21. Blessinger M, Manin J, Skeen SA, Meijer M, Parrish S and Pickett LM. Quantitative mixing measurements and stochastic variability of a vaporizing gasoline direct-injection spray. *Int J Engine Res* 2015; 16: 238–252.

22. Sphicas P, Pickett LM, Skeen SA and Frank JH. Inter-plume aerodynamics for gasoline spray collapse. *Int J Engine Res* 2018; 19: 1048–1067.

23. Pickett LM. Sandia National Laboratories—Engine Combustion Network, https://ecn.sandia.gov/ (2017, accessed 26 February 2019)

24. Hamzah A, Poursadegh F, Lacey J, Petersen P, Brear M and Gordon R. A comparison of diffuse back-illumination (DBI) and Mie-scattering technique for measuring the liquid length of severely flashing spray. In: *20th Australasian Fluid Mechanics Conference (AFMC)*, Perth, Western Australia, Australia, 5–8 December 2016. Victoria, Australia: Australasian Fluid Mechanics Society.

25. Itani LM, Bruneaux G, Hermant L and Schulz C. Investigation of the mixing process and the fuel mass concentration fields for a gasoline direct-injection spray at ECN Spray G conditions and variants. SAE technical paper 2015-01-1902, 2015.

26. Lacey J, Poursadegh F, Brear MJ and Schulz C. Generalizing the behavior of flash-boiling, plume interaction and spray collapse for multi-hole, direct injection. *Fuel* 2017; 200: 345–356.

27. Manin J, Jung Y, Skeen SA, Pickett LM, Parrish SR and Markle L. Experimental characterization of DI gasoline injection processes. SAE technical paper 2015-01-1894, 2015.

28. Montanaro A and Allocca L. Flash boiling evidences of a multi-hole GDI Spray under engine conditions by Mie-scattering measurements. SAE technical paper 2015-01-1945, 2015.

29. Montanaro A, Allocca L and Lazzaro M. Iso-octane Spray from a GDI multi-hole injector under non- and flash boiling conditions. SAE technical paper 2017-01-2319, 2017.

30. Westlye FR, Penney K, Ivarsson A, Pickett LM, Manin J and Skeen SA. Diffuse back-illumination setup for high temporally resolved extinction imaging. *Appl Opt* 2017; 56: 5028–5038.

31. Payri R, Salvador FJ, Martí-Aldaraví P and Vaquerizo D. ECN Spray G external spray visualization and spray collapse description through penetration and morphology analysis. *Appl Therm Eng* 2017; 112: 304–316.

32. Bensing D. *Aufbau eines optisch zugänglichen Einzylinder-Viertaktmotors und charakterisierende Messungen*. PhD thesis, University of Duisburg-Essen, Duisburg, Germany, 2013.

33. Schild M. *Quantitative Untersuchungen zur Zylinderinnenströmung, Gasphasentemperatur und frühen Flammenausbreitung mittels bildgebender Messtechniken*. PhD thesis, University of Duisburg-Essen, Duisburg, Germany, 2016.

34. Kranz P and Kaiser SA. LIF-based imaging of preferential evaporation of a multi-component gasoline surrogate in a direct-injection engine. *Proc Combust Inst* 2019; 37: 1365–1372.

35. Kranz P, Schulz C and Kaiser SA. LIF-based visualization of preferential evaporation of a multi-component fuel in an SIDI engine. In: *8th European combustion meeting*, Dubrovnik, 18–21 April 2017. Pittsburg, USA: The Combustion Institute.

36. Baum E, Peterson B, Böhm B and Dreizler A. On the validation of LES applied to internal combustion engine flows: part 1: comprehensive experimental database. *Flow, Turbul Combust* 2014; 92: 269–297.

37. Jung Y, Manin J, Skeen S and Pickett L. Measurement of liquid and vapor penetration of diesel sprays with a variation in spreading angle. SAE technical paper 2015-01-0946, 2015.

38. Menser J, Schneider F, Dreier T and Kaiser SA. Multi-pulse shadowgraphic RGB illumination and detection for flow tracking. *Exp Fluids* 2018; 59: 90.

39. Laven P. MiePlot program, www.philiplaven.com/mie plot.htm (2018, accessed 24 February 2019).

40. Siebers DL. Liquid-phase fuel penetration in diesel sprays. SAE technical paper 980809, 1998.